Enhanced work hardening from oxygen-stabilized ω precipitates in an aged metastable β Ti-Nb alloy

Kathleen Chou[a], Nan Li[b], Emmanuelle A. Marquis[a*]

[a] *Department of Materials Science and Engineering, University of Michigan, Ann Arbor, MI 48109 USA*

[b] *Center for Integrated Nanotechnologies, MPA Division, Los Alamos National Laboratory, Los Alamos, NM 87545 USA*

**Corresponding Author*

Kathleen Chou
Dow Building
2300 Hayward St.
Ann Arbor, MI 48109
kachou@umich.edu
Phone: 248-925-7880
ORCID: 0000-0003-1974-4766

Nan Li
Los Alamos, NM 87545
nanli@lanl.gov
Phone: (505) 665-1857
ORCID: 0000-0002-8248-9027

Emmanuelle A. Marquis (Corresponding Author)
Dow Building
2300 Hayward St.
Ann Arbor, MI 48109
emarq@umich.edu
Phone: 734-764-8717
ORCID: 0000-0002-6476-2835

Enhanced work hardening from oxygen-stabilized ω precipitates in an aged metastable β Ti-Nb alloy

Kathleen Chou[a], Nan Li[b], Emmanuelle A. Marquis[a*]

[a] *Department of Materials Science and Engineering, University of Michigan, Ann Arbor, MI 48109 USA*

[b] *Center for Integrated Nanotechnologies, MPA Division, Los Alamos National Laboratory, Los Alamos, NM 87545 USA*

**Corresponding Author*

Graphical Abstract

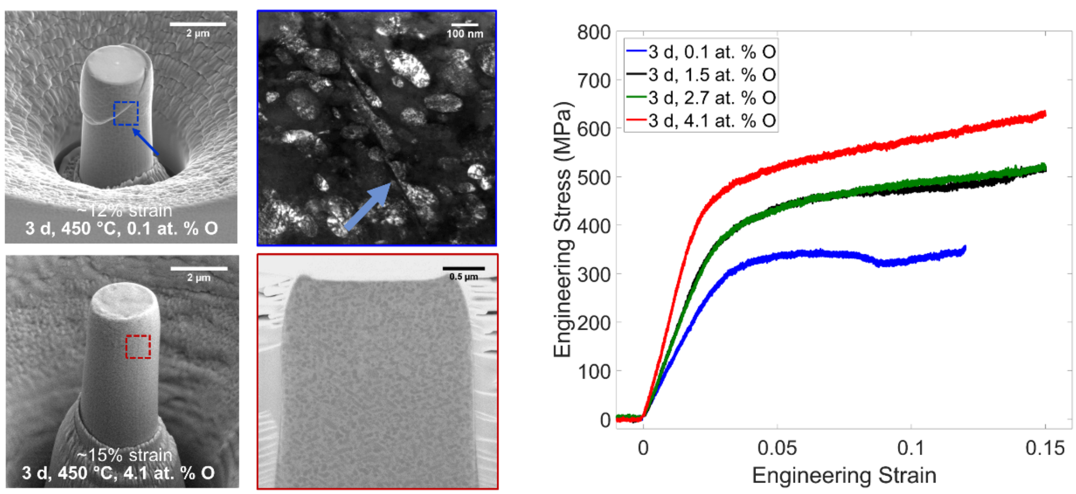

Abstract

High levels of oxygen in solid solution in Ti alloys are considered detrimental to mechanical properties because of embrittlement concerns. In metastable β titanium alloys, the formation of isothermal ω precipitates is also known to cause severe embrittlement and ductility reduction. However, oxygen has been shown to partition to the ω phase during ageing, and this partitioning behavior may potentially impact ω's mechanical contribution. Using micropillar compression, we compared the deformation behavior of Ti-20Nb (at. %) with oxygen-stabilized ω precipitates to the behavior of oxygen-free specimens. The oxygen-stabilized microstructures showed increased compressive yield strength and enhanced work hardening behavior compared to oxygen-free specimens. In the absence of oxygen, the compressed pillars showed slip band formation and catastrophic failure, and transmission electron microscopy imaging revealed that ω precipitates were sheared within the continuous deformation channels resulting in slip localization. In contrast, oxygen-stabilized ω precipitates were harder to shear and the formation of continuous deformation channels was suppressed during compression, leading to improved work hardening behavior up to 15% strain. This counter-intuitive role of oxygen may offer design strategies to address the significant embrittlement and loss of ductility observed for ω-strengthened β Ti alloys without oxygen and avenues to expand the use of β Ti alloys.

Keywords

Titanium alloys, Precipitation, Omega phase, Compression test, Oxygen

1. Introduction

Metastable β titanium alloys that have been developed for aerospace and biomedical structural applications offer a desirable combination of properties including high specific strength and stiffness, biocompatibility, and corrosion resistance [1,2]. These alloys, which typically include significant amounts of β stabilizing elements such as Nb, Mo, and V, characteristically contain a metastable body-centered cubic (bcc) β phase matrix at room temperature [2]. Via thermomechanical processing treatments, the β phase can transform into additional metastable phases that include martensites α' (hexagonal close packed - hcp) and α" (orthorhombic) [2,3], ω phase (hexagonal) [4], or recently reported nanoscale phases [5–10]. Additionally, phase separation resulting from spinodal decomposition or the precipitation of the stable α phase (hcp) may also occur depending on alloy chemistry and processing [1,2]. The wide range of possible microstructures obtained through processing and heat treatment of β Ti alloys allows for the ability to tailor their deformation behavior. Extensive studies have explored the link between phase stability and mechanical behavior in these alloys [2].

Formation of the metastable ω phase during processing of β Ti alloys significantly influences the alloy's deformation mechanisms and structural properties. In Ti alloys, the ω phase is observed in a limited range of alloy compositions at ambient pressures where the stability of the β phase has been increased by adding β stabilizing elements [4]. However, ω may be suppressed in alloy compositions that include minor elements such as Al, Sn, and Zr [11], which are commonly present in commercial alloys, or in stable β alloys with sufficiently high amounts of β stabilizers such that the β transus is below room temperature [2,12]. The orientation relationship between the β and ω phases has been experimentally determined as $\{111\}_{\beta}$ // $(0001)_{\omega}$; $\langle 1\text{-}10\rangle_{\beta}$ // $\langle 11\text{-}20\rangle_{\omega}$ [4], and the ω phase is described as athermal or isothermal depending on alloy composition and formation pathway. In β Ti alloys where the martensite start temperature is lower than the ω start temperature, athermal ω forms rapidly during solution treatment and quenching through a displacive partial collapse of $\{111\}_{\beta}$ planes in the bcc β phase structure [4]. In more solute-rich alloys, precipitation of isothermal ω phase subsequently occurs during ageing at temperatures below about 500 °C. During ageing, a complete collapse of the $\{111\}_{\beta}$ planes takes place to form the hexagonal structure of the isothermal ω phase [4,13] and β-stabilizing elements are rejected from the growing ω precipitates and diffuse to the β phase matrix [14]. Isothermal ageing therefore typically results in high volume fractions of metastable ω precipitates [4,15]. However, prolonged low temperature ageing below ~500 °C eventually yields equilibrium α phase precipitation [2].

Microstructures with extensive isothermal ω formation typically result in reduced ductility and brittle mechanical properties [2,16]. Early literature shows that ω forms as small, coherent particles [16] which are sheared by moving dislocations leading to inhomogeneous slip and embrittlement [17–19]. Therefore, ω precipitation has been historically undesirable for structural applications, and commercial heat treatment practices for β Ti alloys are usually designed to avoid ω formation [12]. However, ω phase formation in β Ti alloys has recently gathered renewed interest due to ω's roles in influencing and controlling deformation behavior. These roles include ω's influence as a heterogeneous nucleation agent for precipitation of the stable α phase [20–22], ability to change transformation-induced plasticity and twinning-induced plasticity deformation mechanisms to dislocation channeling [23], and contribution to enhancing ~~ductility while preserving high~~ strength during short ageing treatments [24,25]. While it is clear that the significant impact of ω precipitates on the deformation behavior of metastable β Ti alloys can be controlled via appropriate ageing, whether the properties of ω precipitates and consequently the mechanical response of β Ti alloys can also be tailored via chemistry is less clear.

Oxygen in solid solution has been shown to change ω's phase stability [26] and significantly influence phase transformations during heat treatment and processing of β Ti alloys [1,2]. In general, titanium has a high affinity for oxygen at room and elevated temperatures [1], and interstitial oxygen has been reported to cause solid solution hardening and reduce ductility for both the α and β phases in Ti [27,28]. However, the ductility of selected β Ti alloys is not reduced with high O levels up to 2.5-3.0 at. % [29,30], which allows for oxygen to be used to tailor microstructural evolution of these alloys. Furthermore, interstitial oxygen changes the formation of metastable phases in β Ti alloys [1,31]. Oxygen has been shown to suppress the martensitic transformation in β titanium alloys during solution treatment and quenching [10,31]. This suppression of martensite reportedly results in novel deformation behavior and thermal expansion properties in gum metal-like compositions [30,32–34]. Oxygen also influences ω and α precipitation during low temperature isothermal ageing [26,35]. During shorter ageing treatments, slight depletion of O in the ω phase has been reported [36]. Additionally, elevated oxygen in Ti-Nb alloys leads to changes in ω's precipitate morphology, number density, and growth rate during ageing, and in α precipitation rate [37]. After extended ageing, oxygen partitions to the ω phase, leaving minimal O present in the β phase matrix [26,35,37]. Although ω precipitates tend to promote shear band formation and slip localization, oxygen's partitioning behavior to ω and its role in refining ω precipitate distributions create an opportunity to investigate the synergy between two detrimental factors, the presence of oxygen and ω formation, on the resulting mechanical properties. Specifically, we show that oxygen-stabilized ω leads to increased resistance to shear localization and consequently to increased strength and strain hardening. The results may suggest design strategies to address the significant embrittlement and loss of ductility observed for ω-strengthened β Ti alloys without oxygen.

2. Experimental

An arc-melted button with a nominal composition of Ti-32.7 wt. % Nb (Ti-20 at. % Nb) was provided by ATI. The button was remelted three times to improve homogeneity. Specimens were cut from the button using a slow speed diamond saw, encapsulated with pure Ti pieces in a quartz tube backfilled with Ar gas, solution treated at 1000 °C for 10 h, and quenched in water. Interstitial oxygen levels were measured in the arc-melted button and after solution-treatment as 0.1 at. % by inert gas fusion using a LECO analyzer. A set of solution treated specimens was oxidized at 900 °C for 5 h in a 1 standard cubic centimeter per minute (SCCM) O_2/4 SCCM Ar environment (approximately $pO_2 = 0.2$ atm/20.3 kPa), which were termed as "pre-oxidized". The as-solution treated specimens and pre-oxidized specimens were subsequently isothermally aged using the following conditions: 300 °C for 3 days or 450 °C for 2 h or 3 days. Oxidation and ageing heat treatments were conducted according to methods reported in Ref. [37]. The aged samples without the oxidation treatment are hereafter referred to as *directly aged* (DA) samples, and the pre-oxidized and aged samples (with the created oxygen gradient) are referred to as *oxidized and aged* (OXA) samples. Investigation at different cross-sectional depths of the OXA specimens corresponded to microstructures with different oxygen contents, which were measured using wavelength dispersive spectroscopy (WDS) as reported in Ref. [37]. Specimens for characterization were mounted in epoxy and ground using 320-1200 grit SiC papers followed by polishing with 0.03 μm colloidal silica suspension. Scanning electron microscopy (SEM) imaging and focused ion beam (FIB) preparation of site-specific transmission electron microscopy (TEM) foils and needle-shaped atom probe tomography (APT) specimens were performed using a Thermo Fisher Scientific FEI Helios 650 Nanolab with a Ga^+ ion FIB. TEM specimens were cleaned using low energy Ar ion milling to remove damage induced during Ga^+ ion FIB milling [38]. TEM images, scanning transmission electron microscopy (STEM) images, and selected area electron diffraction (SAED) patterns were obtained using a JEOL 3011 microscope operated at 300 kV and Thermo Fisher Scientific Talos F200X G2 microscope operated at 200 kV. APT data collection was performed with a Cameca local electrode atom probe (LEAP) 5000 XR operated in laser mode. APT data was collected using a specimen temperature of 30 K, a detection rate of 0.005 atoms per pulse, laser pulse energy of 25 pJ, and pulse repetition rate of 200 kHz. Data reconstruction, background subtraction, peak deconvolution, and compositional analysis were performed using the Integrated Visualization and Analysis Software (IVAS) package 3.8.2 and AP Suite software package 6.1.

Given the compositional gradient and resulting microstructural variation of OXA Ti-20Nb specimens, micropillar compression testing was utilized to probe deformation mechanisms of localized regions within samples. Precise crystallographic grain orientations were measured using electron backscatter diffraction (EBSD) for polished DA and OXA samples. Large β phase grains (approximately 500 μm to 1 mm in size) observed in polished specimens were selected for circular micropillar fabrication (**Supplementary Material**). One grain in each sample was selected with an out-of-plane $(100)_\beta$ orientation to ensure a high Schmid factor for the reported operative $\langle 111\rangle\{112\}_\beta$ slip system for uniaxial compression of ω-enriched β Ti alloys [39,40].

Representative Schmid factor maps calculated from EBSD inverse pole figure (IPF) maps for uniaxial compression with <111>$\{112\}_\beta$ slip and <111>$\{110\}_\beta$ slip are shown in **Supplementary Material**. Although micropillar compression may show size-related effects based on pillar dimensions and tested microstructures [41], precipitate-strengthened alloys with fine precipitate sizes have shown a much weaker size dependence, where deformation behavior is controlled by internal microstructural length scales that dominate over specimen size effects [42,43]. In general, extrinsic size effects tend to dominate when specimen dimensions are sufficiently larger than dispersed microstructural features and the tested volume contains ample dislocation sources [44]. Under such conditions, small-scale mechanical testing methods yield meaningful yield strength values [44]. Therefore, single crystal micropillars with 2 or 5 μm diameters (*d*) were fabricated using FIB and SEM in a Thermo Fisher Scientific FEI Helios 650 Nanolab in order to better approximate bulk-like properties. FIB micropillar fabrication was performed using an automated script with coarse annular milling at 30 kV, 9 nA and fine milling at 30 kV, 0.79 nA. Milled micropillars had a diameter-to-height aspect ratio of approximately 1 to 2.5 to avoid a triaxial stress state for low aspect ratios and pillar buckling at high aspect ratios [45], and micropillars had a maximum vertical taper angle of ~3° due to the Ga^+ ion beam profile [46]. Representative 2 and 5 μm diameter circular pillars are shown in **Supplementary Material**. For OXA specimens, micropillars were fabricated at distances of approximately 100, 500, and 1000 μm from the α lath/β matrix interface, corresponding to oxygen levels of 4.1, 2.7, and 1.5 at. % O, respectively, as measured by WDS [37].

Compression of the micropillars was performed using in-situ and ex-situ systems. In-situ testing was performed using a Bruker/Hysitron PI 85 SEM Picoindenter with a diamond flat punch indenter (11 μm diameter flat end) in a Thermo Fisher Scientific FEI Magellan SEM. Ex-situ testing was performed using a Bruker/Hysitron TI 950 Triboindenter equipped with a flat punch indenter (60° cone angle, 10 μm diameter flat end) or a spherical probe indenter (60° cone angle, 50 μm diameter spherical indenter). Loading was displacement-controlled with a constant loading rate of 2.5 nm/s , resulting in a strain rate of ~0.0005 s^{-1}. Since there may not be an obvious failure point for micropillar compression testing, tests were manually stopped at a predetermined displacement amount in order to characterize compressed pillars at specific nominal strain levels. Videos collected during in-situ compression testing in the SEM show the progression of micropillar deformation for specific conditions and are reported in **Supplementary Material**.

Buckling was not observed for any tested micropillars in this study. Additionally, compression of 2 and 5 μm diameter pillars and using different probe indenter geometries indicated no difference in observed experimental trends (**Supplementary Material**). Engineering stress and strain values were calculated from in-situ and ex-situ load versus displacement data. The engineering stress was calculated as $\sigma = F/A_0$ where F is the measured force and A_0 is the cross-sectional area at the top of the pillar, and the engineering strain was calculated as $\varepsilon = \Delta L/L_0$ where ΔL is the displacement and L_0 is the initial pillar height [40]. During in-situ testing and after ex-situ testing, the morphology of compressed pillars was observed using SEM, TEM, and high-angle annular dark-field (HAADF) STEM imaging of deformed pillars using cross-sectional FIB liftouts similar to Ref. [47].

3. Results

3.1 Initial microstructures of aged Ti-20Nb with varying oxygen content

The aged microstructures for DA and OXA Ti-20Nb specimens were characterized using SEM, TEM, and APT prior to micropillar compression testing to determine differences in precipitate size, number density, and chemistry. The oxidized Ti-20Nb microstructures prior to ageing and detailed discussion of oxygen's role on ω and α precipitation kinetics were reported in Ref. [37]. After isothermal ageing for 3 d at 300 °C, secondary phase precipitates were identified as the ω phase by electron diffraction and formed in the β phase matrix of DA and OXA Ti-20Nb specimens (**Figures 1a-b**). SAED patterns of the $[110]_\beta$ zone axis for both DA and OXA specimens showed ω reflections at 1/3 and 2/3 $\{112\}_\beta$ positions. These ω reflections correspond to the diffraction spots for the ω1 and ω2 variants out of four total ω-variants that form from β. Diffraction spots for the ω3 and ω4 variants are not observed since they are overlapping with the diffraction spots for the β phase [40]. Dark-field TEM images formed by selecting an ω diffraction spot revealed that DA and OXA Ti-20Nb specimens both showed a high number density of ω precipitates distributed homogeneously throughout the β matrix (**Figure 1a-b**). ω's size, aspect ratio, area density, volume fraction, and inter-particle spacing are listed in **Table 1**. The average lengths of the major and minor axes for ω were used to calculate an equivalent spherical diameter, $2r$, for ω precipitates, which were ~4-6 nm regardless of oxygen content. The measured aspect ratio of ω particles based on the major and minor axes increased slightly without oxygen present.

Neglecting particles below 1 nm, ω particles were counted in **Figure 1a-b** for DA and OXA specimens, and then multiplied by 4 to account for the four crystallographic ω variants that form with equal population to obtain the total ω particle count. The average area densities n_s of ω were then estimated by dividing the total particle count by the area of the TEM images in **Figure 1a-b**. The area fraction of ω was estimated using image thresholding and measurement of TEM images using ImageJ processing software to be approximately 11% for both DA and OXA specimens. These area fractions were assumed to equal the volume fraction, f, of ω based on stereology [48]. We note however that the area fraction and therefore the volume fraction may be slightly overestimated by counting particles also located under the surface of the specimen. Finally, the inter-particle spacing D for ω particles was calculated by taking into account the effect of finite obstacle size for impenetrable particles and represents the measure of the free spacing between finite obstacles [49]. The average planar radius $<r_s>$ was calculated using $< r_s > = \pi < r >/4$, which was then used to calculate D using the following equation [49]:

$$D = [(32/3\pi f)^{1/2} - 2] < r_s > \text{(**Equation 1**)}.$$

Although elemental partitioning during ageing is known to occur following ω formation [26], APT measurements for OXA Ti-20Nb with 4.1 at. % O aged for 3 d at 300 °C did not display strong partitioning behavior, as shown by the lack of solute-rich and solute-depleted regions in the reconstructed APT dataset shown in **Figure 1c**. A proximity histogram (or proxigram) that represents a concentration profile as a function of distance from the β/ ω interface was generated using an iso-density surface of 34.2 % Ti, which showed slight concentration differences between the ω and β phases with respect to Ti and Nb indicating the onset of partitioning for these elements (**Figure 1d**). However, interstitial oxygen was still present in both the β and ω phases at approximately 2.2 at. %. These results suggest that elemental partitioning of Ti, Nb, and O has begun, but extensive partitioning has not yet occurred after ageing at 300 °C.

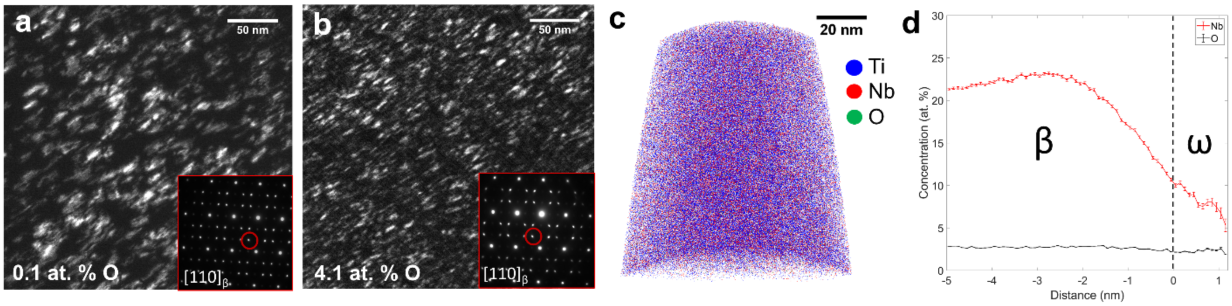

Figure 1. Dark-field TEM images of Ti-20Nb aged for 3 d at 300 °C with (a) 0.1 at. % O and (b) 4.1 at. % O. Insets show SAED patterns for the $[110]_{\beta}$ zone axis showing β and ω diffraction spots. Dark-field images were formed using selected ω diffraction spot in red circle shown in inset. (c) APT reconstruction of OXA Ti-20Nb aged for 3 d at 300 °C with 4.1 at. % O and (d) proxigram showing Nb and O concentration as a function of distance from 34.2 % Ti iso-density surfaces.

Table 1. Quantification of initial microstructural features for ω precipitates in aged Ti-20Nb with varying oxygen content.

Specimen	Ageing Treatment	Oxygen Concentration (at. %)	Equivalent Diameter, *2r,* (nm)	Aspect Ratio	Area Density, n_s (um^{-2})	Volume Fraction, *f*	Inter-particle spacing, *D* (nm)
DA	3 d, 300 °C	0.1	6.1	3.0	12837	0.11	8.6
OXA	3 d, 300 °C	4.1	4.5	2.5	28877	0.11	6.3
DA	2 h, 450 °C	0.1	33	2.8	1457	0.34	15
OXA	2 h, 450 °C	4.1	27	3.8	1796	0.34	12
DA	3 d, 450 °C	0.1	115	1.6	88	0.45	34
OXA	3 d, 450 °C	1.5	110	1.6	84	0.45	32
OXA	3 d, 450 °C	2.7	104	1.9	102	0.45	31
OXA	3 d, 450 °C	4.1	86	3.9	127	0.45	25

Ageing times at 450 °C and oxygen levels were selected to clarify the influence of elevated oxygen on ω precipitation kinetics and morphologies. After ageing for 2 h at 450 °C, ω precipitates grew in size, and the DA and OXA microstructures showed fine ~30 nm ω precipitates with partitioned elements as evidenced from high compositional contrast in backscattered SEM (SEM-BSE) images (**Figure 2a-b**). SEM-BSE images also showed a higher number density and elongated precipitate morphologies for ω with elevated oxygen levels. Previous TEM imaging had revealed that a more elongated and rod-like shape was observed for ω precipitates aged for 2 h at 450 °C with elevated O compared to ellipsoidal shapes with minimal oxygen [37]. Similar quantifications for ω's size, aspect ratio, area density, volume fraction, and inter-particle spacing were obtained for DA and OXA specimens after ageing for 2 h at 450 °C (**Table 1**). For these specimens, ω's size, area density, and volume fraction were estimated using SEM-BSE images that showed all ω variants. In particular, the aspect ratio for ω in OXA Ti-20Nb with 4.1 at. % O is higher than for DA specimens without oxygen, which reflects the elongated shape of ω that develops with oxygen. The volume fraction for ω precipitates increased to ~34% for DA and OXA specimens. APT measurements were also conducted to investigate the extent of elemental partitioning after ageing at 450 °C. A reconstructed APT dataset for OXA Ti-20Nb with 4.1 at. % O (**Figure 2c**) showed strong elemental partitioning as well as Ti-rich regions and Nb-rich regions corresponding to the ω and β phase, respectively. Furthermore, proxigram measurements using a 77 at. % Ti iso-concentration surface showed up to 6 at. % O in the ω phase and ~1 at. % O in the β phase (**Figure 2d**). Therefore, oxygen partitioned to the ω phase after ageing at 450 °C, leaving low levels of oxygen present in the β matrix. Such elemental partitioning behavior is consistent with ageing results reported for similar Ti-Nb-O containing alloys [26,35,37], and is also consistent with oxygen acting as an ω-stabilizer for Ti-Nb alloys [37]. The lack of oxygen partitioning between β and ω after ageing at 300 °C when Nb has already noticeably partitioned to β (**Figure 1d**) is puzzling considering that interstitial oxygen typically diffuses faster than Nb in Ti [27,50]. However, our results are consistent with previous findings. Little partitioning (**Figure 1d**) or depletion of oxygen in ω has been found for aged β Ti alloys at lower temperatures and/or with short ageing times resulting in nanometer-sized ω particles [36], while significant oxygen partitioning has been reported for ageing conditions that promote larger ω precipitates shown in (**Figure 2d**) and Refs. [26,35].

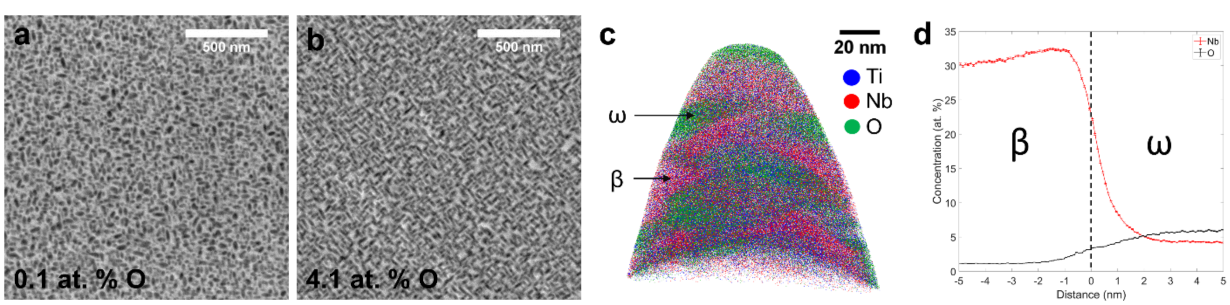

Figure 2. SEM-BSE images of Ti-20Nb aged for 2 h at 450 °C with (a) 0.1 at. % O and (b) 4.1 at. % O. (c) APT reconstruction of OXA Ti-20Nb aged for 2 h at 450 °C with 4.1 at. % O and (d) proxigram showing Nb and O concentration as a function of distance from 77 at. % Ti iso-concentration surfaces.

Prolonged ageing for 3 d at 450 °C resulted in continued growth and coarsening of ω precipitates at all oxygen levels. SEM-BSE images and bright-field TEM observations showed changes in ω's size, number density, and morphology related to oxygen content (**Figure 3** and **Table 1**). The OXA specimens with elevated oxygen content exhibited a higher number density of ω precipitates than the DA specimens without oxygen, and the shape of ω precipitates changed from ellipsoidal to rod-like with increasing oxygen levels. Such changes are consistent with previously reported results for Ti-Nb alloys with elevated oxygen [37]. The volume fraction of ω precipitates after 3 d of ageing for both DA and OXA specimens at all oxygen levels was approximately 45%, which is likely the maximum volume fraction for this alloy at 450 °C. Regardless of oxygen content, no α phase was noted after ageing for 3 d at 450 °C. Additionally, as expected from prior work [26], significant elemental partitioning was observed, with the β and ω phases being rich in Nb and Ti, respectively. For OXA specimens, oxygen partitioned to the ω phase up to 6 at. % during isothermal ageing and minimal oxygen of ~0.3 at. % O was present in the β matrix, in accordance with previously reported ω partitioning behavior [26,37] and ω stabilization with oxygen [37].

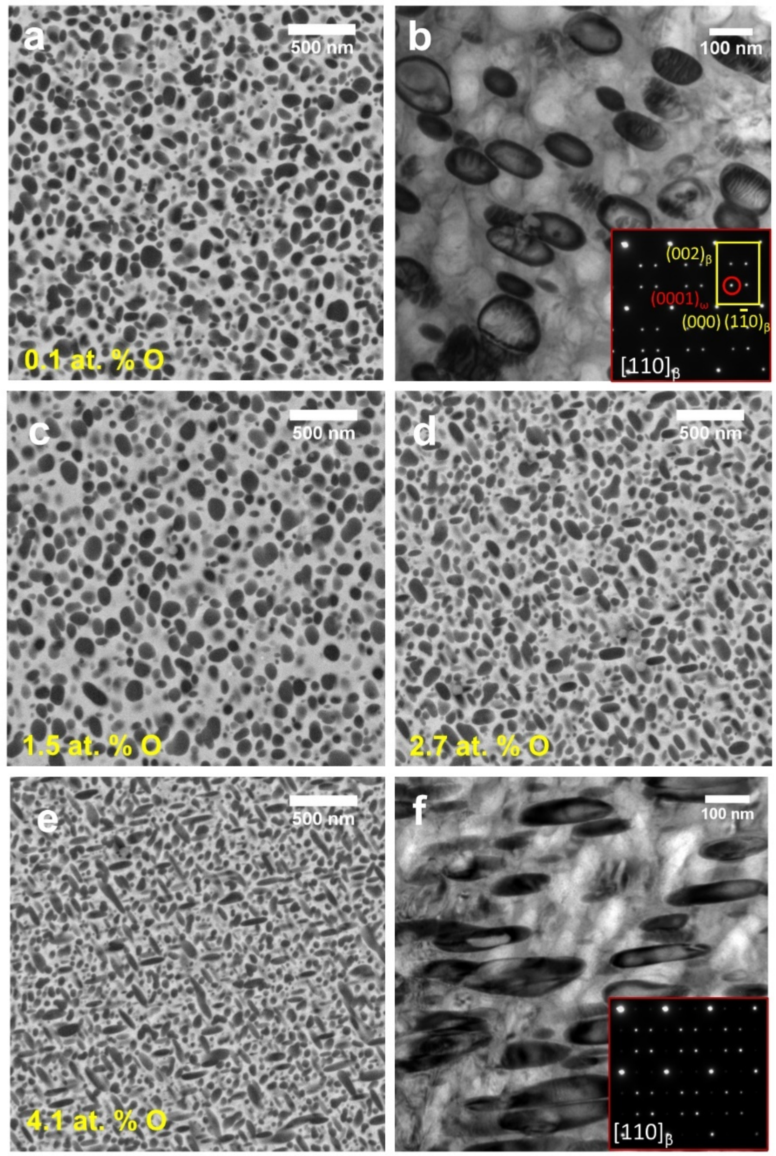

Figure 3. (a) SEM-BSE and (b) bright-field TEM images of Ti-20Nb aged for 3 d at 450 °C with 0.1 at. % O. SEM-BSE images of Ti-20Nb aged for 3 d at 450 °C with (c) 1.5, (d) 2.7, and (e) 4.1 at. % O. (f) Bright-field TEM image of Ti-20Nb aged for 3 d at 450 °C with 4.1 at. % O. Insets for bright-field TEM images in (b) and (f) show SAED patterns for the $[110]_\beta$ zone axis showing β and ω diffraction spots.

3.2 Micropillar compression and deformed microstructures of Ti-20Nb aged at 300 °C

Micropillar compression testing of DA and OXA specimens aged at 300 °C was conducted to determine the deformation behavior of microstructures with a high number density of nanometer-sized ω precipitates and interstitial oxygen that has not yet strongly partitioned to ω. Post-compression images of 2 μm diameter pillars for Ti-20Nb with 0.1 or 4.1 at. % O aged for 3 d at 300 °C deformed to 15-20% strain showed a large number of slip bands regardless of oxygen content (**Figure 4a-b**). In-situ observations showed slip band formation and fast catastrophic pillar failure for both DA and OXA micropillars (**Supplementary Material**). The associated compressive engineering stress-strain curves showed that serrated flow and several large drops in stress values were observed after initial yielding for both DA and OXA specimens (**Figure 4c**). In-situ compression testing revealed that the observed load drops matched the activation of macro-scale slip events on favorable slip planes (**Supplementary Material**). The similarity in behavior for the DA and OXA micropillars aged at 300 °C suggests that elevated oxygen levels did not affect the deformation mode.

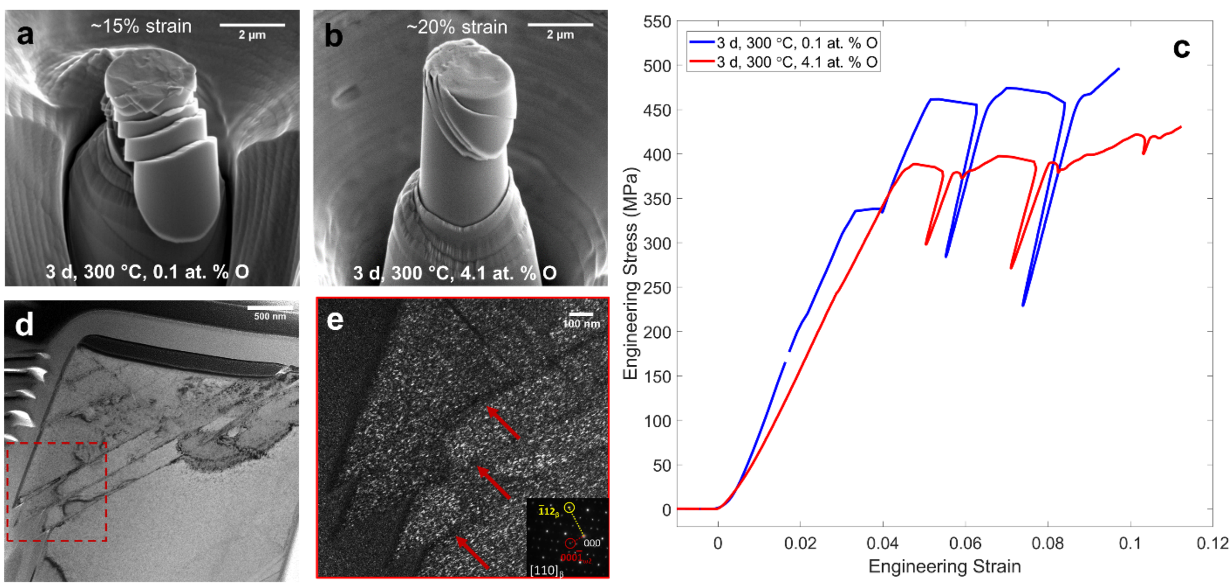

Figure 4. SEM-BSE images of compressed micropillars for Ti-20Nb aged for 3 d at 300 °C with (a) 0.1 at. % O and (b) 4.1 at. % O. (c) Engineering stress-strain curves for compressed micropillars in (a) and (b). (d) Bright-field and (e) dark-field TEM images of liftout sample from compressed pillar with 4.1 at. % O in (b) showing depleted ω precipitates and precipitate free channels (red arrows).

In order to evaluate the deformed microstructure, TEM imaging was performed on liftout samples from cross-sections along $[110]_\beta$ for a deformed pillar from Ti-20Nb with 4.1 at. % O aged for 3 d at 300 °C. Several parallel slip bands were observed spanning the pillar's width (**Figure 4d**) and the ω phase was depleted in the slip bands (**Figure 4e**), resulting in the formation of precipitate-free channels located in the slip bands. Slip trace analysis of the slip bands revealed that the bands were parallel to the $(-112)_\beta$ plane consistent with dislocation activity occurring on the $<111>\{112\}_\beta$ slip system. These results suggest that the removal of ω precipitates is related to localized dislocation slip that accounts for slip band formation. Similar observations of localized dislocation activity, removal of ω precipitates along the <111>{112}$_{\beta}$ slip system, and formation of precipitate-free channels have been reported in several other β Ti alloys containing nanometer-sized ω with and without oxygen [17,23,39,40]. In particular, micropillar compression of β Ti-10V-2Fe-3Al alloy with nanometer-sized ω precipitates reported the formation of precipitate-free channels with localized dislocation slip that resulted in serrated flow and load drops observed during micropillar compression testing [40].

3.3 Micropillar compression and deformed microstructures of Ti-20Nb aged at 450 °C

To determine differences in mechanical properties and deformation behavior with varying oxygen content, micropillar compression testing was also performed for DA and OXA specimens aged at 450 ℃ for 3 days such that elemental partitioning to the ω precipitates and β matrix occurred. Without oxygen present, macroscopic slip bands readily formed across the pillars (**Figure 5a**, **Supplementary Material**). However, with increasing oxygen levels, the formation of slip bands after compression was gradually suppressed, and micropillars with 2.7 and 4.1 at. % O did not show any step formation or slip bands after compression (**Figure 5c-d**, **Supplementary Material**). A similar series of micropillar compression tests was conducted for DA and OXA specimens aged for only 2 hours so that they contained finer ω precipitates. Comparable trends with increasing oxygen content were observed for compressed micropillars from specimens that were aged for 2 hours (**Figure 5e-f**). Micropillars for the DA specimen without oxygen showed several slip bands after deformation (**Figure 5e**). In contrast, deformed pillars for the OXA sample with 4.1 at. % O showed fewer slip bands with smaller step features (**Figure 5f**), and comparing the pillar's shape before and after compression showed slight bulging that suggests more distributed deformation. The significant reduction in the size and number of slip bands formed with increasing oxygen for these pillars also supports the observation of suppressed slip bands for deformed micropillars with high oxygen after 450 °C ageing.

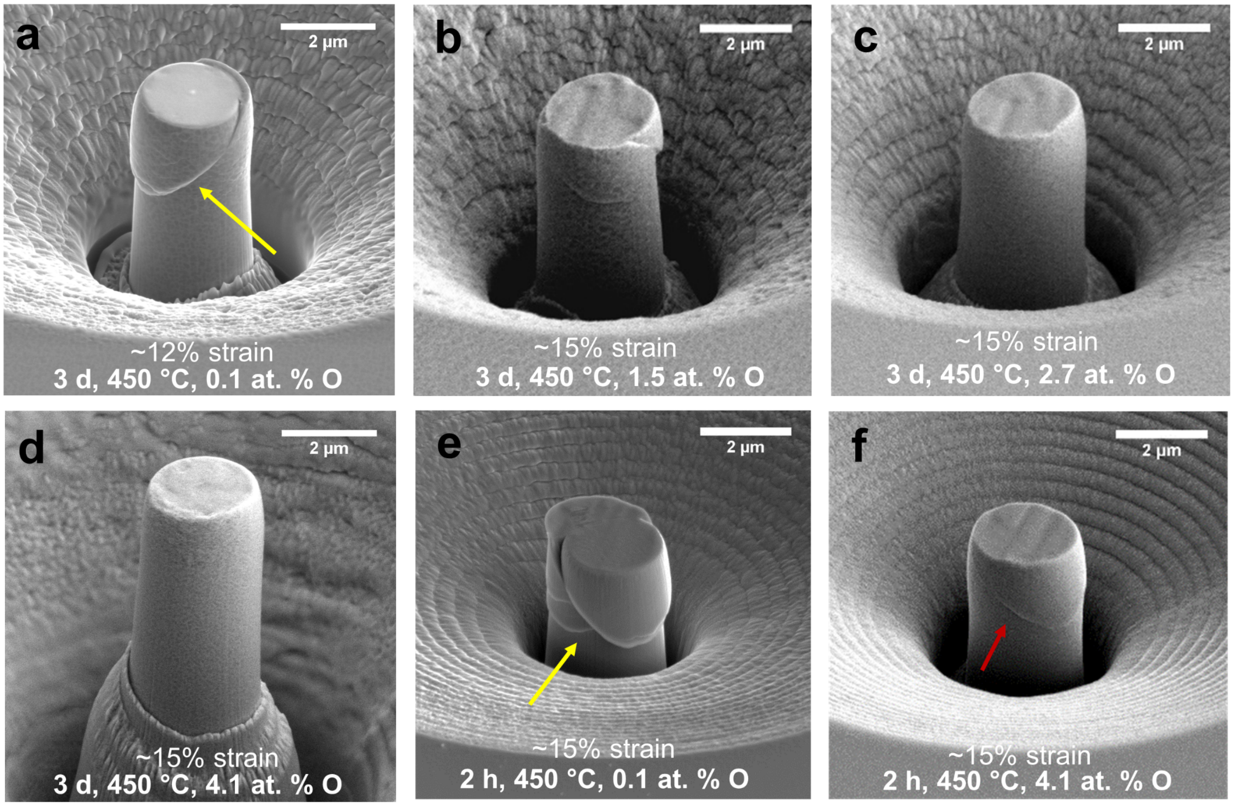

Figure 5. SEM-BSE images of compressed micropillars for Ti-20Nb aged for 3 d at 450 °C with (a) 0.1, (b) 1.5, (c) 2.7, and (d) 4.1 at. % O, and for Ti-20Nb aged for 2 h at 450 °C with (e) 0.1 and (f) 4.1 at. % O. Yellow and red arrows show slip bands formed on micropillars during compression testing.

Compressive engineering stress-strain curves up to 15% strain calculated from the collected load versus displacement data during compression of DA and OXA specimens aged for 3 d at 450 °C were plotted to evaluate the influence of ω's size, number density, and oxygen content (**Figure 6a**). In the absence of oxygen, the stress-strain curve showed a flat curve after initial yielding and a drop in the stress with increasing strain, which corresponded to macro-scale slip band and step formation (**Supplementary Material**). In contrast, the stress-strain curves for pillars fabricated on the OXA specimen with higher oxygen contents exhibited smooth and continuous flow, as well as increased work hardening after initial yielding. The average compressive yield strengths and standard deviation values based on 0.2% offset values of four tested micropillars for each condition were approximately 294 ± 10, 358 ± 5, 364 ± 7, and 464 ± 26 MPa for the DA specimen without oxygen and the OXA specimen with 1.5, 2.7, and 4.1 at. % O, respectively. Therefore, comparing the DA specimen without O and OXA specimen with 1.5 at. % O revealed that yield strength increased with higher oxygen levels for the same ω size. For OXA Ti-20Nb with 2.7 and 4.1 at. %

O, the higher oxygen levels and more refined ω sizes likely both contributed to the observed increases in yield strengths. Changes in strain hardening behavior were evaluated using true stress-true strain curves for micropillars tested on DA and OXA specimens. Strain hardening behavior is given by Ludwik's equation [51]:

$$\sigma = \sigma_0 + K\varepsilon^n \text{ (}\textbf{Equation 2}\text{)}$$

where σ_0 is the initial yield stress, K is the strengthening coefficient, and n is the strain hardening exponent. Strain hardening exponents for compressed micropillars were estimated by fitting the plastic region of true stress-true strain curves to **Equation 2** for specimens aged for 3 d at 450 °C. For the DA specimen that showed a load drop in the stress-strain curve, n was calculated based on the plastic region up to the onset of the first load drop corresponding to slip band formation (located at blue arrow in **Figure 6a**). Notably, the average and standard deviation values for the strain hardening exponent n were approximately 0.12 ± 0.03 for the DA specimen without O and 0.25 ± 0.02 for the OXA specimen with 1.5, 2.7, and 4.1 at. % O, respectively, based on four tested micropillars per condition, confirming the increase in work hardening for OXA specimens with higher oxygen. These trends were also observed in engineering stress-strain curves for DA and OXA micropillars aged for 2 h at 450 °C (**Figure 6b**). More instability in the stress-strain curve was observed for DA micropillars aged for 2 h (blue curve in **Figure 6b**) attributed to the activation of more slip bands that was observed for these deformed pillars compared to pillars after 3 d of ageing (**Figure 5a** and **Figure 5e**). With high oxygen content, stress-strain curves for micropillars fabricated on OXA specimens aged for 2 h with 4.1 at. % O exhibited similar yield strength values and work hardening capability as those with coarser ω precipitates aged for 3 d with 4.1 at. % O.

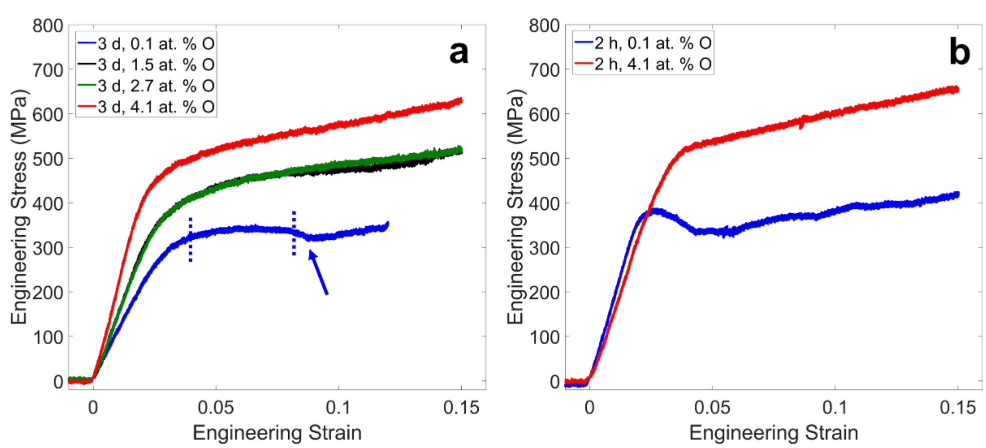

Figure 6. (a) Engineering stress-strain curves for compressed micropillars from Ti-20Nb aged for 3 d at 450 °C with varying oxygen content. Dashed lines in (a) show regions used for fitting to Equation 2 to estimate strain hardening exponents for

micropillars with a load drop (located at blue arrow). (b) Engineering stress-strain curves for compressed micropillars from Ti-20Nb aged for 2 h at 450 °C with 0.1 and 4.1 at. % O.

After compression, micropillars were cross-sectioned along $[110]_\beta$ and examined using SEM and TEM to observe the deformed microstructures. SEM imaging of a compressed micropillar deformed to ~15% strain for DA specimens without O aged for 3 days at 450 °C was consistent with ω precipitate shearing, and a slip band that propagated across the entire pillar diameter suggested significant localized deformation (**Figure 7a**). Dark-field TEM images formed using ω reflections showed a continuous slip band that cut through ω precipitates (**Figure 7b**). Similar to deformed microstructures after 300 °C ageing, the slip bands are consistent with dislocation activity on the $<111>\{112\}_\beta$ slip system. The larger sizes of ω after 450 °C ageing prevented the complete disappearance of ω precipitates after shearing, but a deformation channel was still formed by shearing of precipitates that propagated in a continuous line across the entire pillar width. Similar ω-free channels have been reported with larger ω precipitates after bulk tensile testing of a Ti-Mo alloy [52]. Therefore, deformation of the oxygen-free pillar for DA Ti-20Nb aged for 3 d at 450 °C resulted in shearing of ω precipitates along the $<111>\{112\}_\beta$ slip system in a continuous channel spanning the entire pillar.

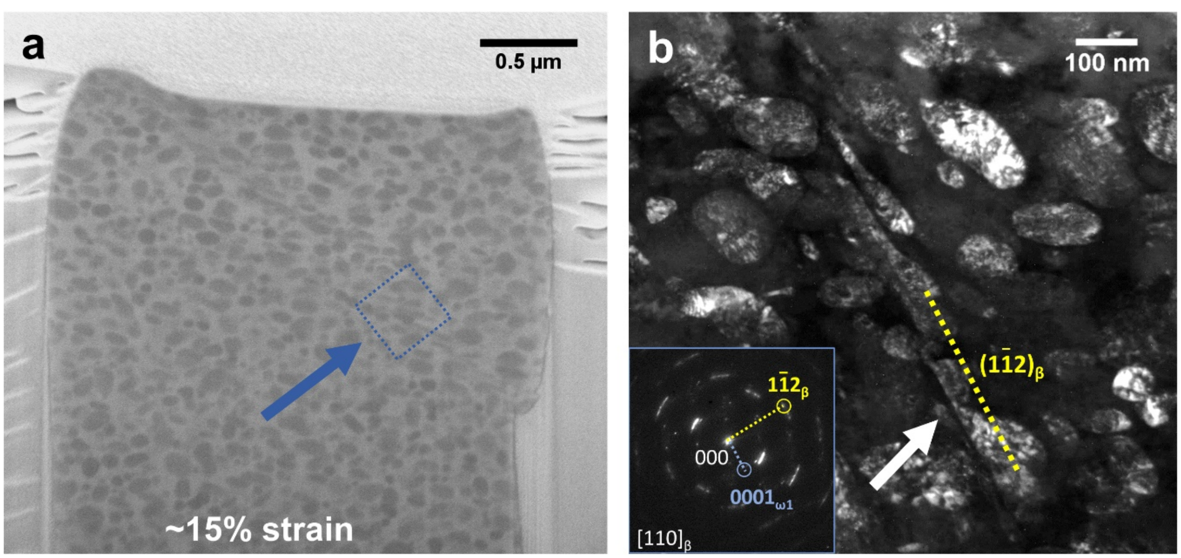

Figure 7. (a) SEM-BSE image of cross-section for compressed micropillar with 15% strain for Ti-20Nb aged for 3 d at 450 °C with 0.1 at. % O. (b) Dark-field TEM image of liftout from blue outlined region in compressed pillar shown in (a). Inset shows TEM SAED pattern. White arrow points to slip bands and sheared ω precipitates along $\{112\}_\beta$ planes.

The higher number density of rod-like ω precipitates in Ti-20Nb aged for 3 d at 450 °C with 4.1 at. % O complicated observation of potential precipitate shearing in FIB cross-sectioned pillars (**Figure 8a**). SEM-BSE images of the cross-sectioned pillar did not show obvious slip band formation or ω shearing after deformation to ~15% strain (**Figure 8a**). HAADF STEM images for a liftout sample with a $[110]_\beta$ zone axis showed that the shape of ω precipitates remained largely intact without obvious channel formation (**Figure 8b**). However, possible indications of precipitate shearing along $\{112\}_\beta$ planes were visible on select ω precipitates (**Figure 8c-d**). These presumably sheared precipitates tended to be isolated features, and no extended shearing across multiple precipitates was observed. Imaging was also conducted for an OXA Ti-20Nb micropillar aged for 2 h at 450 °C with 4.1 at. % O to understand the deformed microstructure with smaller ω precipitates that still showed significant chemical partitioning. HAADF STEM images of a cross-sectioned liftout for a deformed pillar to 15% strain also revealed regions with isolated shearing of ω precipitates aligned with the $<111>\{112\}_\beta$ slip system (located at pairs of red arrows in **Figure 9**), but no extended shearing was observed. While ω precipitates can still be sheared with elevated oxygen, the formation of a continuous channel spanning the entire pillar's diameter that results in localized deformation was hindered.

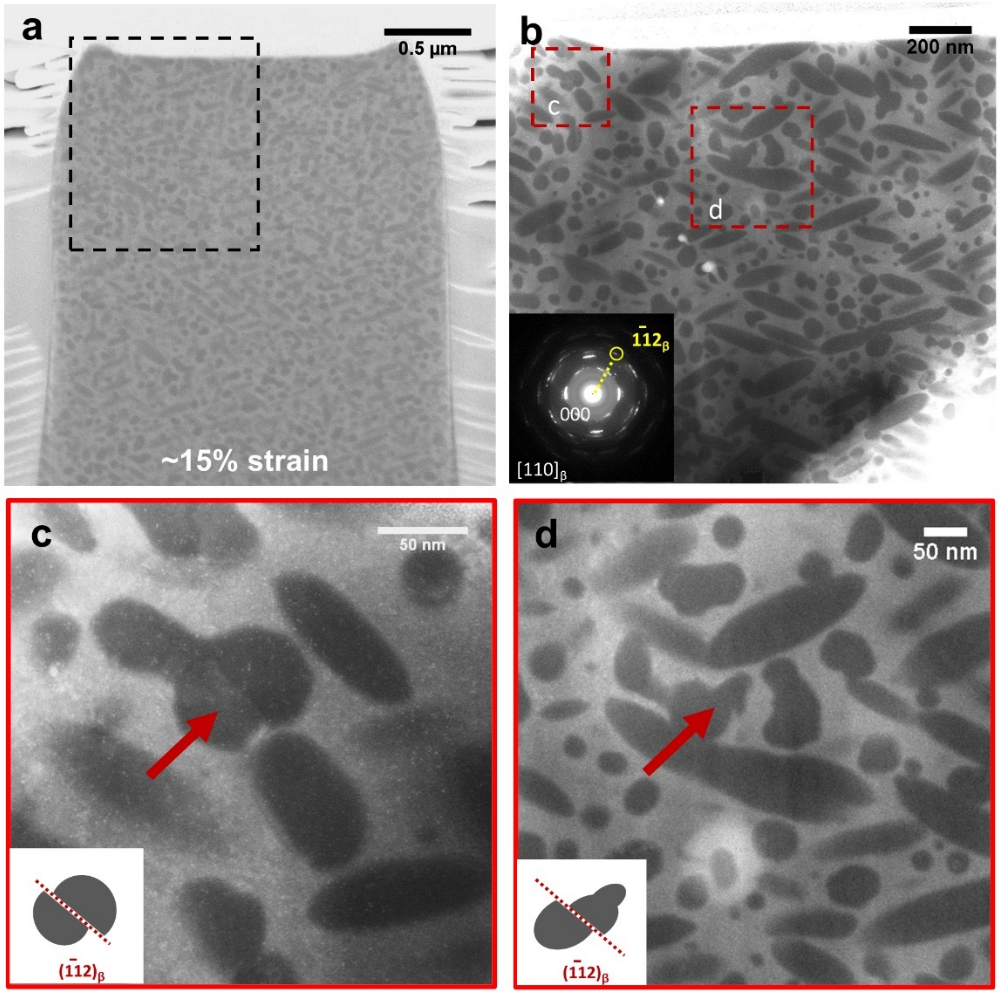

Figure 8. (a) SEM-BSE image of cross-section for compressed micropillar with 15% strain for Ti-20Nb aged for 3 d at 450 °C with 4.1 at. % O. (b) HAADF STEM image of black outlined region in compressed pillar shown in (a). Inset shows TEM SAED pattern. (c-d) Higher magnification images of (b) with inset showing schematic diagram of precipitate shearing. Red arrows point to sheared ω precipitates along $\{112\}_\beta$ planes.

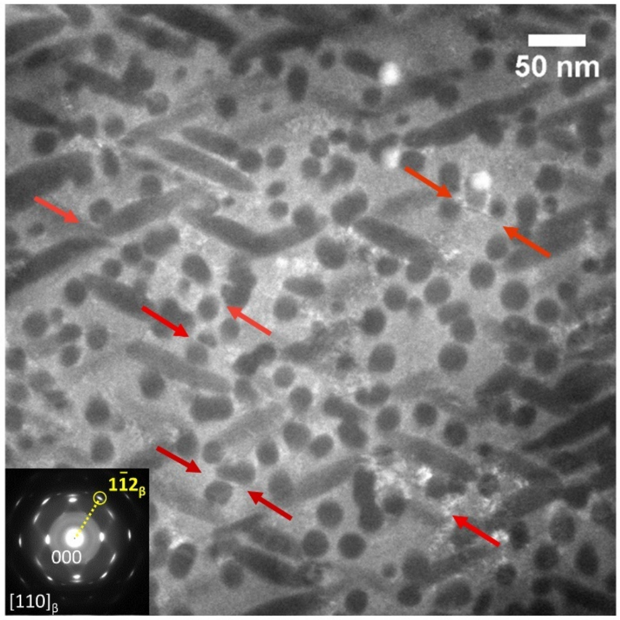

Figure 9. HAADF STEM image of liftout sample from compressed micropillar with 15% strain for Ti-20Nb aged for 2 h at 450 °C with 4.1 at. % O. Pairs of arrows colored in shades of red show regions with sheared ω precipitates.

4. Discussion

Micropillar compression testing of elevated oxygen and oxygen-free microstructures in aged metastable β Ti-20Nb alloys showed significant changes in deformation behavior and mechanical properties depending on initial microstructures and oxygen content. In specimens with nanometer-sized ω (smaller than ~6 nm), compression testing resulted in the formation of shear bands, and engineering stress-strain curves showed serrated flow and several load drops regardless of oxygen content. In specimens with larger ω sizes (50-120 nm), the oxygen content strongly influenced the deformation response and the associated compressive stress-strain data. In the absence of oxygen, compression testing resulted in the formation of shear bands and low work hardening. In contrast, the presence of 2.7 and 4.1 at. % O suppressed shear band formation, while the associated stress-strain curves showed enhanced work hardening after initial yielding, even though the microstructures consisted of known embrittling features in the form of interstitial oxygen and metastable ω phase formation.

Precipitate shearing, slip localization deformation mechanisms, and fast catastrophic failure in β Ti alloys containing ω precipitates is not unexpected. Similar observations have been reported for several nominally oxygen-free β Ti alloys after bulk [17,18,23] and micropillar [40,53–55] testing. The ω phase formed during quenching or very short ageing, where significant elemental partitioning has not yet taken place, generally does not result in loss of ductility [24,25,52]. However, upon isothermal ageing, increased tensile strengths with reduced ductility are typically observed [2]. The loss of ductility has been attributed to the ω structural transition from trigonal to hexagonal and the onset of solute partitioning, both contributing to the hardening of ω precipitates and suppression of twinning [53]. Differences in shear modulus between β and ω may also account for the suppression of transformation-induced plasticity and twinning-induced plasticity deformation mechanisms [23]. Deformation then occurs by shearing of coherent ω particles resulting in planar slip and formation of localized slip bands [17], primarily on the $\langle 111 \rangle \{112\}_{\beta}$ slip system [39], leading to negligible work hardening and fast fracture. The onset of localized slip is associated with the formation of dislocation channels [23,39]. The deformation mode is thought to be controlled by the deformation anisotropy of ω variants, in which one of the four variants is easily sheared but the other three variants show strong lattice resistance to dislocation slip [40]. However, as dislocations pile up, all variants are eventually sheared through ω lattice dissolution [40,53]. With these mechanisms, the removal of ω precipitates creates softer channels that concentrate and limit plastic flow in narrow slip bands leading to fracture [17,39,40]. These deformation mechanisms operate for a wide range of ω precipitate sizes ranging from several nanometers [17,23,39,40] to 100-200 nm [17,52].

The investigated microstructures aged at 300 and 450 °C showed a wide range of ω sizes related to ageing conditions and oxygen content that changed the growth kinetics for ω (**Table 1**). To understand the relative roles of precipitate size and oxygen level in suppressing shear band formation, the average and standard deviation of yield strengths based on four tested micropillars for each condition were plotted against ω's equivalent diameter (**Figure 10**). For ω particles with an equivalent diameter smaller than 10 nm, corresponding to Ti-20Nb aged at 300 °C, pillars without oxygen showed a lower average yield point value compared to pillars with elevated O, which is consistent with similar ω-containing microstructures for β Ti alloys that showed increases in yield strength with higher O in bulk tensile testing [39]. The large error bars for yield points at these ω sizes are attributed to the stochastic nature of the triggering events for fast catastrophic failure and possible size-related contributions from micropillar compression testing [43]. At equivalent diameters between 20-40 nm corresponding to specimens aged at 450 °C for 2 h, micropillars containing oxygen showed a significant increase in yield strength while the strengths for those without oxygen remained constant or decreased. With equivalent diameters increasing above 80 nm for specimens aged at 450 °C for 3 d, the yield strength decreased with larger ω sizes for both oxygen-containing and oxygen-free pillars, and the oxygen-containing micropillars maintained higher yield strengths than those of oxygen-free pillars.

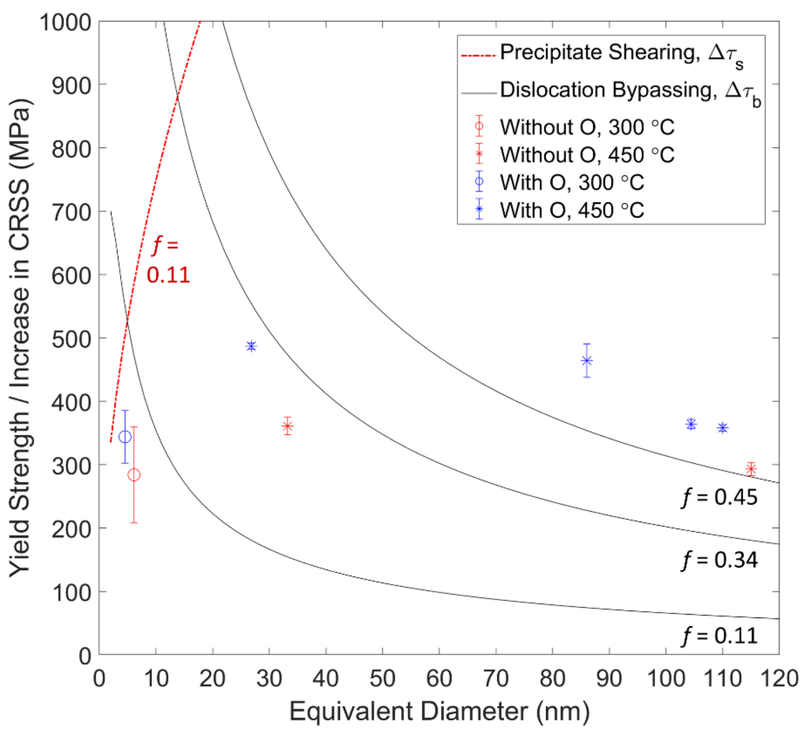

Figure 10. Average compressive yield strength dependence on ω equivalent diameter for tested micropillars and calculated stresses for precipitate shearing and dislocation bypassing mechanisms for aged Ti-20Nb with and without interstitial oxygen.

The transition in yield strength dependence with oxygen at ~10 nm equivalent diameters for ω suggests a change in the dislocation interactions. Dislocations are known to shear through coherent ω particles or bypass them through Orowan looping [17]. The increase in critical resolved shear stress (CRSS) for ω precipitate shearing from modulus strengthening was estimated using the following equation [56]:

$$\Delta\tau_s = A(|\Delta G|)^{3/2}\left(\frac{fr}{Gb}\right)^{1/2} \quad \textbf{(Equation 3)}$$

where A is a constant that was approximated as 0.013, ΔG the difference in shear modulus between ω precipitates and the β matrix, f the volume fraction of ω particles, $2r$ the equivalent diameter for ω, G the shear modulus of the β matrix, and b the Burgers vector of the β matrix. The increase in CRSS due to a dislocation bypassing mechanism through Orowan looping was also estimated for the investigated microstructures using the following equation [17,57]:

$$\Delta\tau_b = \frac{1}{1-\nu}\frac{Gb}{2\pi D} ln\frac{\sqrt{2/3}r}{b}$$ (**Equation 4**)

where D is the inter-particle spacing. The values of Poisson's ratio v and G of the β phase have been estimated for a similar Ti-Nb based gum metal alloy as 0.39 and 25 GPa, respectively, using single crystal elastic constants measured with in-situ synchrotron x-ray diffraction [39,58]. The value of G for single-crystalline ω phase was estimated for pure Ti as 60 GPa [59]. Assuming the same values for Ti-20Nb and using the microstructural parameters given in **Table 1**, $\Delta\tau_s$ and $\Delta\tau_b$ were calculated using the observed volume fractions in the initial ω microstructures (**Figure 10**). $\Delta\tau_s$ for f = 0.34 and f = 0.45 are not shown, but such a high volume fraction would lead to even higher stresses for precipitate shearing. Importantly, the smaller applied stress for these two mechanisms transitions from precipitate shearing to dislocation bypassing at ω equivalent diameters of ~10 nm for f = 0.11, which is a similar value to the transition size noted for the experimental data (**Figure 10**). Furthermore, the stresses for dislocation bypassing estimated using f = 0.34 and f = 0.45 are lower than that of precipitate shearing for these volume fractions. Although these estimates for $\Delta\tau_s$ and $\Delta\tau_b$ provide only relative comparisons for the stresses required to activate these mechanisms, this simple analysis suggests that precipitate shearing is easiest for nanometer-sized ω in Ti-20Nb aged at 300 °C, while dislocation bypassing becomes possible at larger ω sizes obtained after ageing at 450 °C. Previous investigations have reported the presence of dislocation loops indicating the activation of dislocation bypassing and Orowan looping for deformed microstructures with larger ω precipitates after bulk tensile testing [16,17]. We now discuss the effect of oxygen with the different ω precipitate sizes.

The mechanical response of specimens aged at 300 °C with nanoscale ω precipitates was similar with and without oxygen. The similar precipitate distributions and the lack of strong chemical partitioning during low temperature ageing suggest that oxygen did not significantly change the nature of the precipitates and consequently the active deformation mechanisms, as was previously observed in related Ti-Nb-O gum metal alloys containing nanometer-sized ω precipitates [39]. Dislocation bypassing and Orowan looping of ω particles is unlikely considering the higher stresses required compared to precipitate shearing. The predominance of shearing with and without oxygen contributed to the formation of precipitate-free channels observed after compression (**Figure 4**), resulting in negligible work hardening and fast failure.

For specimens containing ω precipitates with equivalent diameters greater than ~10-30 nm depending on the specific ω volume fraction, dislocation bypassing of ω particles becomes feasible. The activation of dislocation bypassing at larger ω sizes can account for the shape of the stress-strain curves of DA specimens without O aged for 3 d at 450 °C (blue curve in **Figure 6a**). Some amount of plastic deformation was observed after initial yielding and prior to load drops that correspond to slip band formation, suggesting that some amount of distributed plasticity via Orowan bypassing is possible before localization and catastrophic failure (**Supplementary Material**). Note that shearing and disordering of 3 of the 4 ω variants requires very high stresses [40], and therefore Orowan bypassing becomes a viable way to account for distributed plasticity. Eventually, shearing and disordering of ω particles leading to formation of a continuous deformation channel still occurred (**Figure 7b**). This suggests that although the stresses to shear ω are quite high at large ω sizes, dislocations pile-up will eventually reach sufficient levels to shear and dissolve ω variants [39,40], which would result in both Orowan bypassing and precipitate shearing mechanisms being activated. This behavior differed significantly from that of micropillars aged at 300 °C where the high stresses required for Orowan bypassing allowed precipitate shearing to be the only possible deformation mechanism, and steep load drops occurred immediately after yielding (**Figure 4** and **Supplementary Material**).

The presence of oxygen that partitioned to larger ω precipitates during the ageing treatment at 450 °C not only contributed to increasing the alloy's yield strength, but also significantly increased the work hardening capability and prevented shear band formation. Oxygen's partitioning behavior from β to ω during ageing, which was also previously noted [26,35,37], results in minimal oxygen in solid solution in the β phase matrix after ageing at 450 °C and mitigates the ductility reduction known to occur with higher oxygen levels for β Ti [27]. Interstitial oxygen in ω may impede dislocation motion along the $<111>\{112\}_\beta$ slip system and improve ω's resistance to precipitate shearing and disordering during deformation. The preferred site for interstitial oxygen atoms in the ω lattice is the octahedral site according to previous density functional theory calculations [60]. Consequently, oxygen in the octahedral site is also in the path of dislocation movement and may directly interfere with the ability of dislocations to pass through or disorder ω variants along the <111>{112}$_\beta$ slip system that promotes the formation of precipitate-free channels and planar slip [39,40]. We note that the presence of oxygen in Ti-Nb-Fe alloys similarly hindered atomic movement and shearing along the same crystallographic system <111>{112}$_\beta$ during martensitic transformation [61]. The presence of oxygen atoms in ω likely increases the critical resolved shear stress required to shear through and disorder ω variants, improving ω's resistance to precipitate shearing. Consequently, dislocations are less likely to continuously shear ω particles to form precipitate-free channels that result in planar slip during deformation leading to fast fracture. Dislocation bypassing of ω precipitates accounts for the homogeneous deformation and improved work hardening observed during compression (**Figure 6**). Oxygen-stabilized ω precipitates with partitioned O at these sizes may therefore behave similar to non-shearable particles, and the deformation of these microstructures during micropillar compression testing would then be controlled by the inter-particle spacing, as has been demonstrated in an oxide dispersion strengthened Ni alloy [42]. It is thus the combination of larger ω sizes that enable dislocation bypassing during deformation and oxygen's partitioning to ω that increases its resistance to precipitate shearing and disordering that lead to the suppression of precipitate-free channels and low work hardening behavior observed for DA Ti-20Nb specimens without oxygen.

These results directly address the structural issues of ω precipitation and embrittlement during ageing of metastable β titanium alloys and may inform subsequent chemistry and heat treatment design strategies to improve and expand the use of β Ti alloys. Furthermore, these findings contradict the conventional wisdom that interstitial oxygen causes embrittlement in Ti alloys and must be kept at low levels. With oxygen-containing compositions, ageing treatments designed to promote ω growth and oxygen partitioning mitigate known challenges of embrittlement from isothermal ω precipitates and interstitial oxygen present in the β matrix. A significant outcome of forming oxygen-stabilized ω with sizes that allow for dislocation bypassing is the suppression of plastic flow localization responsible for severe embrittlement and poor ductility of ω-strengthened β Ti alloys without oxygen. This behavior combined with the high yield strengths generally observed for microstructures containing isothermal ω precipitates may enable new opportunities to develop new types of β Ti alloy chemistries and processing that intentionally utilize oxygen as a beneficial alloying element.

5. Conclusions

Micropillar compression studies of aged Ti-20Nb specimens with varying oxygen content were investigated to understand the effect of oxygen partitioning to ω on compressive deformation behavior. The following conclusions were drawn:

1) Ti-20Nb (at. %) aged at 300 and 450 °C showed extensive ω precipitation irrespective of oxygen content. For the same ageing condition, high oxygen levels slowed the growth kinetics for ω, resulting in higher number densities of smaller ω precipitates in samples with elevated O compared to specimens without O. In oxygen-containing specimens up to 4.1 at. % O, oxygen partitioned to ω precipitates from the β matrix for aged samples at 450 °C, but little oxygen partitioning was observed for those aged at 300 °C.
2) Different oxygen levels did not change the deformation behavior and deformed pillar morphologies of Ti-20Nb aged at 300 °C. Compressed pillars showed slip bands on pillar surfaces, serrated flow in stress-strain curves, and the formation of precipitate-free channels in post-deformation TEM imaging regardless of oxygen content. These results are attributed to precipitate shearing and disordering of the nanometer-sized ω precipitates present after ageing at 300 °C that contributed to the formation of precipitate-free channels, slip localization, and fast fracture of compressed pillars.
3) Elevated oxygen content significantly changed the compressed micropillar morphologies and engineering stress-strain curve shapes for Ti-20Nb aged at 450 °C containing larger ω precipitates. Deformed pillars without oxygen showed large slip bands on pillar surfaces and negligible work hardening with load drops in stress-strain curves. In contrast, slip band formation was suppressed for tested pillars with elevated oxygen that formed oxygen-stabilized ω precipitates, and stress-strain curves showed improved work hardening with smooth, continuous plastic flow after initial yielding. These differences with oxygen content are attributed to oxygen's partitioning to ω during ageing that improved ω's resistance to precipitate shearing and impeded the formation of continuous deformation channels, which allowed for dislocation bypassing and homogeneous deformation resulting in improved work hardening behavior.

4) Microstructures with oxygen-stabilized ω precipitates offer significant benefits and pathways for future development of metastable β Ti alloys by mitigating two known challenges for embrittlement from interstitial oxygen impurities and isothermal ω formation.

Acknowledgements

This work was supported by the National Science Foundation (NSF) through grants NSF DMR-1436154 and CMMI-1729166, and the Graduate Research Fellowship Program under grant No. DGE 1256260. This work was performed, in part, at the Center for Integrated Nanotechnologies, an Office of Science User Facility operated for the U.S. Department of Energy (DOE) Office of Science. Los Alamos National Laboratory, an affirmative action equal opportunity employer, is managed by Triad National Security, LLC for the U.S. Department of Energy's NNSA, under contract 89233218CNA000001. The authors acknowledge financial and technical support from the University of Michigan Center for Materials Characterization. Additional travel support was provided through a Rackham Graduate Student Research Grant from the University of Michigan. The authors would also like to thank Dr. John Foltz (ATI), Dr. Allen Hunter (U. Michigan), and Dr. Haiping Sun (U. Michigan) for providing the Ti-20Nb button, development of automated script for micropillar fabrication, and assistance with micropillar compression testing.

References

[1] D. Banerjee, J.C. Williams, Perspectives on Titanium Science and Technology, Acta Mater. 61 (2013) 844–879. https://doi.org/10.1016/j.actamat.2012.10.043.

[2] R. Kolli, A. Devaraj, A Review of Metastable Beta Titanium Alloys, Metals (Basel). 8 (2018) 506. https://doi.org/10.3390/met8070506.

[3] M. Bönisch, A. Panigrahi, M. Calin, T. Waitz, M. Zehetbauer, W. Skrotzki, J. Eckert, Thermal stability and latent heat of Nb–rich martensitic Ti-Nb alloys, J. Alloys Compd. 697 (2017) 300–309. https://doi.org/10.1016/j.jallcom.2016.12.108.

[4] S. Banerjee, R. Tewari, G.K. Dey, Omega phase transformation – morphologies and

mechanisms, Int. J. Mater. Res. 97 (2006) 963–977. https://doi.org/10.3139/146.101327.

[5] Y. Zheng, D. Banerjee, H.L. Fraser, A nano-scale instability in the β phase of dilute Ti–Mo alloys, Scr. Mater. 116 (2016) 131–134. https://doi.org/10.1016/j.scriptamat.2016.01.044.

[6] H.L. Wang, Y.L. Hao, S.Y. He, T. Li, J.M. Cairney, Y.D. Wang, Y. Wang, E.G. Obbard, F. Prima, K. Du, S.J. Li, R. Yang, Elastically confined martensitic transformation at the nano-scale in a multifunctional titanium alloy, Acta Mater. 135 (2017) 330–339. https://doi.org/10.1016/j.actamat.2017.06.040.

[7] Q. Liang, Y. Zheng, D. Wang, Y. Hao, R. Yang, Y. Wang, H.L. Fraser, Nano-scale structural non-uniformities in gum like Ti-24Nb-4Zr-8Sn metastable β-Ti alloy, Scr. Mater. 158 (2019) 95–99. https://doi.org/10.1016/j.scriptamat.2018.08.043.

[8] Y. Zheng, S. Antonov, Q. Feng, R. Banerjee, D. Banerjee, H.L. Fraser, Shuffle-induced modulated structure and heating-induced ordering in the metastable β-titanium alloy, Ti-5Al-5Mo-5V-3Cr, Scr. Mater. 176 (2020) 7–11. https://doi.org/10.1016/j.scriptamat.2019.09.027.

[9] Y. Zheng, R.E.A. Williams, S. Nag, R. Banerjee, H.L. Fraser, D. Banerjee, The effect of alloy composition on instabilities in the β phase of titanium alloys, Scr. Mater. 116 (2016) 49–52. https://doi.org/10.1016/j.scriptamat.2016.01.024.

[10] M. Tahara, H.Y. Kim, T. Inamura, H. Hosoda, S. Miyazaki, Lattice modulation and superelasticity in oxygen-added β-Ti alloys, Acta Mater. 59 (2011) 6208–6218. https://doi.org/10.1016/j.actamat.2011.06.015.

[11] J.C. Williams, B.S. Hickman, D.H. Leslie, The effect of ternary additions on the decompositon of metastable beta-phase titanium alloys, Metall. Trans. 2 (1971) 477–484. https://doi.org/10.1007/bf02663337.

[12] J.D. Cotton, R.D. Briggs, R.R. Boyer, S. Tamirisakandala, P. Russo, N. Shchetnikov, J.C. Fanning, State of the Art in Beta Titanium Alloys for Airframe Applications, Jom. 67 (2015) 1281–1303. https://doi.org/10.1007/s11837-015-1442-4.

[13] B.S. Hickman, The formation of omega phase in titanium and zirconium alloys: A review, J. Mater. Sci. 4 (1969) 554–563. https://doi.org/10.1007/bf00550217.

[14] A. Devaraj, S. Nag, R. Srinivasan, R.E.A. Williams, S. Banerjee, R. Banerjee, H.L. Fraser, Experimental evidence of concurrent compositional and structural instabilities leading to ω precipitation in titanium–molybdenum alloys, Acta Mater. 60 (2012) 596–609. https://doi.org/10.1016/j.actamat.2011.10.008.

[15] B.S. Hickman, Omega Phase Precipitation in Alloys of Titanium with Transition Metals, Trans TMS-AIME. 245 (1969) 1329–1336.

[16] J.C. Williams Hickman, B.S., Marcus, H.L., The effect of omega phase on the mechanical properties of titanium alloys, Metall. Trans. 2 (1971) 1913–1919. https://doi.org/10.1007/BF02913423.

[17] A. Gysler, G. Lütjering, V. Gerold, Deformation behavior of age-hardened Ti-Mo alloys, Acta Metall. 22 (1974) 901–909. https://doi.org/10.1016/0001-6160(74)90057-1.

[18] T.W. Duerig, G.T. Terlinde, J.C. Williams, Phase transformations and tensile properties of Ti-10V-2Fe-3AI, Metall. Trans. A. 11 (1980) 1987–1998. https://doi.org/10.1007/bf02655118.

[19] J.C. Sabol, C.J. Marvel, M. Watanabe, T. Pasang, W.Z. Misiolek, Confirmation of the ω-phase in electron beam welded Ti–5Al–5V–5Mo–3Cr by high-resolution scanning transmission electron microscopy: An initial investigation into its effects on embrittlement, Scr. Mater. 92 (2014) 15–18. https://doi.org/10.1016/j.scriptamat.2014.08.003.

[20] Y. Zheng, R.E.A. Williams, J.M. Sosa, Y. Wang, R. Banerjee, H.L. Fraser, The role of the ω phase on the non-classical precipitation of the α phase in metastable β-titanium alloys, Scr. Mater. 111 (2016) 81–84. https://doi.org/10.1016/j.scriptamat.2015.08.019.

[21] T. Li, D. Kent, G. Sha, L.T. Stephenson, A. V Ceguerra, S.P. Ringer, M.S. Dargusch, J.M. Cairney, New insights into the phase transformations to isothermal ω and ω-assisted α in near β-Ti alloys, Acta Mater. 106 (2016) 353–366. https://doi.org/10.1016/j.actamat.2015.12.046.

[22] T. Li, D. Kent, G. Sha, H. Liu, S.G. Fries, A. V Ceguerra, M.S. Dargusch, J.M. Cairney, Nucleation driving force for ω-assisted formation of α and associated ω morphology in β-Ti alloys, Scr. Mater. 155 (2018) 149–154. https://doi.org/10.1016/j.scriptamat.2018.06.039.

[23] M.J. Lai, T. Li, D. Raabe, ω phase acts as a switch between dislocation channeling and joint twinning- and transformation-induced plasticity in a metastable β titanium alloy, Acta Mater. 151 (2018) 67–77. https://doi.org/10.1016/j.actamat.2018.03.053.

[24] J. Gao, A.J. Knowles, D. Guan, W.M. Rainforth, ω phase strengthened 1.2GPa metastable β titanium alloy with high ductility, Scr. Mater. 162 (2019) 77–81. https://doi.org/10.1016/j.scriptamat.2018.10.043.

[25] F. Sun, J.Y. Zhang, P. Vermaut, D. Choudhuri, T. Alam, S.A. Mantri, P. Svec, T. Gloriant, P.J. Jacques, R. Banerjee, F. Prima, Strengthening strategy for a ductile metastable β-titanium alloy using low-temperature aging, Mater. Res. Lett. 5 (2017) 547–553. https://doi.org/10.1080/21663831.2017.1350211.

[26] M. Niinomi, M. Nakai, M. Hendrickson, P. Nandwana, T. Alam, D. Choudhuri, R. Banerjee, Influence of oxygen on omega phase stability in the Ti-29Nb-13Ta-4.6Zr alloy, Scr. Mater. 123 (2016) 144–148. https://doi.org/10.1016/j.scriptamat.2016.06.027.

[27] Z. Liu, G. Welsch, Effects of oxygen and heat treatment on the mechanical properties of alpha and beta titanium alloys, Metall. Trans. A. 19 (1988) 527–542. https://doi.org/10.1007/bf02649267.

[28] H. Conrad, Effect of interstitial solutes on the strength and ductility of titanium, Prog.

Mater. Sci. 26 (1981) 123–403. https://doi.org/10.1016/0079-6425(81)90001-3.

[29] V. Jablokov, N. Murray, H. Rack, H. Freese, Influence of Oxygen Content on the Mechanical Properties of Titanium-35Niobium-7Zirconium-5Tantalum Beta Titanium Alloy, J. ASTM Int. 2 (2005) 12776. https://doi.org/10.1520/JAI12776.

[30] T. Saito, T. Furuta, J.H. Hwang, S. Kuramoto, K. Nishino, N. Suzuki, R. Chen, A. Yamada, K. Ito, Y. Seno, T. Nonaka, H. Ikehata, N. Nagasako, C. Iwamoto, Y. Ikuhara, T. Sakuma, Multifunctional Alloys Obtained via a Dislocation-Free Plastic Deformation Mechanism, Science (80-.). 300 (2003) 464–467. https://doi.org/10.1126/science.1081957.

[31] W. Weng, A. Biesiekierski, Y. Li, C. Wen, Effects of selected metallic and interstitial elements on the microstructure and mechanical properties of beta titanium alloys for orthopedic applications, Materialia. 6 (2019) 100323. https://doi.org/10.1016/j.mtla.2019.100323.

[32] L.S. Wei, H.Y. Kim, S. Miyazaki, Effects of oxygen concentration and phase stability on nano-domain structure and thermal expansion behavior of Ti–Nb–Zr–Ta–O alloys, Acta Mater. 100 (2015) 313–322. https://doi.org/10.1016/j.actamat.2015.08.054.

[33] L.S. Wei, H.Y. Kim, T. Koyano, S. Miyazaki, Effects of oxygen concentration and temperature on deformation behavior of Ti-Nb-Zr-Ta-O alloys, Scr. Mater. 123 (2016) 55–58. https://doi.org/10.1016/j.scriptamat.2016.05.043.

[34] P. Castany, A. Ramarolahy, F. Prima, P. Laheurte, C. Curfs, T. Gloriant, In situ synchrotron X-ray diffraction study of the martensitic transformation in superelastic Ti-24Nb-0.5N and Ti-24Nb-0.5O alloys, Acta Mater. 88 (2015) 102–111. https://doi.org/10.1016/j.actamat.2015.01.014.

[35] T. Homma, A. Arafah, D. Haley, M. Nakai, M. Niinomi, M.P. Moody, Effect of alloying elements on microstructural evolution in oxygen content controlled Ti-29Nb-13Ta-4.6Zr (wt%) alloys for biomedical applications during aging, Mater. Sci. Eng. A. 709 (2018) 312–321. https://doi.org/10.1016/j.msea.2017.10.018.

[36] M.J. Lai, T. Li, F.K. Yan, J.S. Li, D. Raabe, Revisiting ω phase embrittlement in metastable β titanium alloys: Role of elemental partitioning, Scr. Mater. 193 (2021) 38–42. https://doi.org/10.1016/j.scriptamat.2020.10.031.

[37] K. Chou, E.A. Marquis, Oxygen effects on ω and α phase transformations in a metastable β Ti–Nb alloy, Acta Mater. 181 (2019) 367–376. https://doi.org/10.1016/j.actamat.2019.09.049.

[38] H.-H. Jin, H.-D. Cho, S. Kwon, C. Shin, J. Kwon, Modified preparation technique of TEM sample for various TEM analyses of structural materials, Mater. Lett. 89 (2012) 133–136. https://doi.org/10.1016/j.matlet.2012.08.069.

[39] M.J. Lai, C.C. Tasan, D. Raabe, Deformation mechanism of ω-enriched Ti–Nb-based gum metal: Dislocation channeling and deformation induced ω–β transformation, Acta Mater.

100 (2015) 290–300. https://doi.org/10.1016/j.actamat.2015.08.047.

[40] W. Chen, J. Zhang, S. Cao, Y. Pan, M. Huang, Q. Hu, Q. Sun, L. Xiao, J. Sun, Strong deformation anisotropies of ω -precipitates and strengthening mechanisms in Ti-10V-2Fe-3Al alloy micropillars: Precipitates shearing vs precipitates disordering, Acta Mater. 117 (2016) 68–80. https://doi.org/10.1016/j.actamat.2016.06.065.

[41] M.D. Uchic, D.M. Dimiduk, J.N. Florando, W.D. Nix, Sample dimensions influence strength and crystal plasticity, Science (80-.). 305 (2004) 986–989. https://doi.org/10.1126/science.1098993.

[42] B. Girault, A.S. Schneider, C.P. Frick, E. Arzt, Strength Effects in Micropillars of a Dispersion Strengthened Superalloy, Adv. Eng. Mater. 12 (2010) 385–388. https://doi.org/10.1002/adem.201000089.

[43] R. Gu, A.H.W. Ngan, Size effect on the deformation behavior of duralumin micropillars, Scr. Mater. 68 (2013). https://doi.org/10.1016/j.scriptamat.2013.02.012.

[44] J.P. Wharry, K.H. Yano, P. V Patki, Intrinsic-extrinsic size effect relationship for micromechanical tests, Scr. Mater. 162 (2019) 63–67. https://doi.org/10.1016/j.scriptamat.2018.10.045.

[45] H. Zhang, B.E. Schuster, Q. Wei, K.T. Ramesh, The design of accurate micro-compression experiments, Scr. Mater. 54 (2006) 181–186. https://doi.org/10.1016/j.scriptamat.2005.06.043.

[46] C. Shin, S. Lim, H. Jin, P. Hosemann, J. Kwon, Development and testing of microcompression for post irradiation characterization of ODS steels, J. Nucl. Mater. 444 (2014) 43–48. https://doi.org/10.1016/j.jnucmat.2013.09.025.

[47] C. Shin, H. h Jin, H. Sung, D.J. Kim, Y.S. Choi, K. Oh, Evaluation of Irradiation Effects on Fracture Strength of Silicon Carbide using Micropillar Compression Tests, Exp. Mech. 53 (2012) 687–697. https://doi.org/10.1007/s11340-012-9678-1.

[48] G. Vander Voort, Measurement of Microstructure, in: Met. Handb. Desk Ed., ASM International, 1998. https://doi.org/10.31399/asm.hb.mhde2.a0003248.

[49] A.J. Ardell, Precipitation hardening, Metall. Trans. A. 16 (1985) 2131–2165. https://doi.org/10.1007/BF02670416.

[50] G.B. Gibbs, D. Graham, D.H. Tomlin, Diffusion in titanium and titanium—niobium alloys, Philos. Mag. 8 (1963). https://doi.org/10.1080/14786436308207292.

[51] Y. Pan, Q. Sun, L. Xiao, X. Ding, J. Sun, Plastic deformation behavior and microscopic mechanism of metastable Ti-10V-2Fe-3Al alloy single crystal pillars orientated to <011>β in submicron scales Part I: Double size effects and martensitic transformation prediction, Mater. Sci. Eng. A. 743 (2019) 798–803. https://doi.org/10.1016/j.msea.2018.11.140.

[52] S.A. Mantri, D. Choudhuri, T. Alam, V. Ageh, F. Sun, F. Prima, R. Banerjee, Change in the deformation mode resulting from beta-omega compositional partitioning in a Ti Mo

alloy: Room versus elevated temperature, Scr. Mater. 130 (2017) 69–73. https://doi.org/10.1016/j.scriptamat.2016.11.013.

[53] W. Chen, S. Cao, W. Kou, J. Zhang, Y. Wang, Y. Zha, Y. Pan, Q. Hu, Q. Sun, J. Sun, Origin of the ductile-to-brittle transition of metastable β-titanium alloys: Self-hardening of ω-precipitates, Acta Mater. 170 (2019) 187–204. https://doi.org/10.1016/j.actamat.2019.03.034.

[54] Y. Pan, H. Wu, X. Wang, Q. Sun, L. Xiao, X. Ding, J. Sun, E.K.H. Salje, Rotatable precipitates change the scale-free to scale dependent statistics in compressed Ti nano-pillars, Sci Rep. 9 (2019) 3778. https://doi.org/10.1038/s41598-019-40526-5.

[55] W. Kou, Q. Sun, L. Xiao, J. Sun, Coupling effect of second phase and phase interface on deformation behaviours in microscale Ti-55531 pillars, J. Alloys Compd. 820 (2020) 153421. https://doi.org/10.1016/j.jallcom.2019.153421.

[56] E. Nembach, Particle Strengthening of Metals and Alloys, Wiley, New York, 1997.

[57] M.F. Ashby, Oxide Dispersion Strengthening, in: G.S. Ansell, T.D. Cooper, F.V. Lenel (Eds.), Gordon & Breach, 1968.

[58] R.J. Talling, R.J. Dashwood, M. Jackson, D. Dye, On the mechanism of superelasticity in Gum metal, Acta Mater. 57 (2009) 1188–1198. https://doi.org/10.1016/j.actamat.2008.11.013.

[59] M. Tane, Y. Okuda, Y. Todaka, H. Ogi, A. Nagakubo, Elastic properties of single-crystalline ω phase in titanium, Acta Mater. 61 (2013) 7543–7554. https://doi.org/10.1016/j.actamat.2013.08.036.

[60] J.G. Niu, D.H. Ping, T. Ohno, W.T. Geng, Suppression effect of oxygen on the β to ω transformation in a β-type Ti alloy: insights from first-principles, Model. Simul. Mater. Sci. Eng. 22 (2014) 15007. https://doi.org/10.1088/0965-0393/22/1/015007.

[61] Y. Fu, W. Xiao, J. Wang, L. Ren, X. Zhao, C. Ma, Oxygen induced crystal structure transition of martensite in Ti–Nb–Fe alloys, Mater. Lett. 262 (2020) 127026. https://doi.org/10.1016/j.matlet.2019.127026.